Quantum-enhanced phased array scheme based on NOON states

Ji-Hong Guo(郭继红)[1], Jun Li(李军)[1]*, Wei-Hao Wang(王炜皓)[1],
Hao Duan(段昊)[1], and Cong-Feng Liu(刘聪锋)[2]

[1]National Key Laboratory of Radar Signal Processing, Xidian University, Xi'an 710071, China
[2]Key Laboratory of Electronic Information Countermeasure and Simulation Technology,
Ministry of Education, Xidian University, Xi'an 710071, China

Abstract

The key advantage of phased array technology lies in its ability to achieve beam steering via beamforming and significantly improve the signal-to-noise ratio (SNR). However, classical phased array, based on the coherent superposition of electromagnetic waves, is constrained by classical physics in both capabilities. In this work, we propose a quantum-enhanced phased array architecture exploiting the quantum coherence of N-photon entangled states. The coherent-state-based phased array (CPA) follows the conventional phased-array beamforming principle, and its beam pattern represents the angular distribution of the average light intensity. In contrast to the CPA, the beam pattern of the NOON-state-based phased array (NPA) represents the angular distribution of the intensity correlation of N entangled photons. Beamforming calculations for the NPA and CPA show that when the NPA forms a normalized beam pattern of the same shape as that of the CPA, the array aperture of the NPA can be reduced by a factor of N compared with that of the CPA. Furthermore, we explore the effects of different parameters on the SNR gains of the NPA and CPA systems, revealing the fundamental differences in their SNR performance. The results show that NPA achieves higher SNR gain than CPA under certain parameter conditions. Finally, calculations based on detection parameters demonstrate that the NPA enables a longer detection range under identical transmit power levels.

Keywords: quantum phased array, NOON state, quantum correlation function
PACS: 42.50.-p, 42.50.St, 03.67.-a

1. Introduction

Radar is a system that acquires target information by transmitting electromagnetic waves into space and processing their reflected echoes. However, classical radars, relying on classical physics principles, are fundamentally constrained in target detection capabilities by classical physical limits. Since the advent of quantum mechanics in the early 20th century [1], researchers have sought to exploit quantum physics to achieve performance beyond classical limits. Notably, such explorations have seen significant advances in quantum information technology, where quantum coherence and entanglement have been exploited to drive key progress in quantum sensing, communication, and computation [2–7].

Quantum radar, an emerging concept in recent years with the advancement of quantum information science, which breaks through the performance limit of classical radar by utilizing quantum resources and quantum technology [8–13]. Among the various quantum-radar protocols, quantum illumination has been the most extensively studied. Its quantum advantage is typically obtained in the low-brightness

*Corresponding author. E-mail: junli01@mail.xidian.edu.cn

regime, where the average signal photon number per spatiotemporal mode is much smaller than unity [14–17]. To extend quantum illumination beyond a single sensing channel, quantum radar arrays and quantum illumination networks employing multiple parallel channels have been proposed. In 2019, Luong et al. [18] conducted some preliminary explorations into the possibility of building quantum radar arrays. Wang et al. [19] explored multiple two-photon entangled sources to enhance signal power and attain improved signal-to-noise ratio (SNR) in 2024. More recently, Zhao et al. [20] proposed a quantum illumination network using multiple two-mode squeezed vacuum (TMSV) states, demonstrating quantum advantages in multi-target detection and parameter estimation. In these architectures, multiple quantum radar units or signal–idler channels operate in parallel, and the quantum enhancement arises primarily from signal–idler correlations and joint processing of the received signals and retained reference modes.

Related advances have also been made in quantum-enhanced sensing and distributed sensor networks. In distributed architectures, quantum resources are shared among spatially separated sensing nodes, and the measurement outcomes from different nodes are jointly processed. Entangled sensor networks have been demonstrated for angle-of-arrival estimation, radio-frequency signal classification, and quantum positioning and ranging [21–23]. Beyond distributed networks, squeezed-light schemes have been applied to enhance radio-frequency signal resolution and optomechanical acceleration sensing [24,25]. Multipartite entanglement has been employed to realize an optomechanical sensor network [26].

Although the quantum radar arrays and distributed quantum sensing schemes discussed above differ in their specific tasks and quantum resources, they generally employ multiple spatial channels to acquire signal information in parallel and jointly process the resulting measurements. In contrast, phased array technology forms a directional beam by controlling the relative phases of the signals emitted by different array elements, so that the radiated fields interfere constructively in a prescribed spatial direction. This enables precise beam steering and improves the output SNR compared with mechanically scanned radars [27]. However, classical phased arrays remain subject to classical limits in beamforming and SNR enhancement. In quantum metrology, the high order interference of NOON states has been widely used to achieve phase sensitivity beyond the standard quantum limit [28–30]. Motivated by this high order quantum coherence, we introduce NOON states into a phased array architecture to explore quantum enhanced beamforming and SNR improvement.

In this paper, we propose a quantum enhanced phased array architecture based on N photon entangled states. By exploiting high order quantum coherence and controlling the phases of individual array elements, the system generates directional beams and realizes beam steering. Using quantum correlation functions, we analyze the beamforming characteristics of the NOON state phased array (NPA) and the coherent state phased array (CPA). The results show that, for identical normalized beam patterns, the NPA reduces the required array aperture by a factor of N compared with the CPA. We further evaluate their SNR gains in noisy environments and show that the NPA can outperform the CPA under specific parameter regimes. Finally, calculations based on representative detection parameters indicate that the NPA can achieve a longer detection range than the CPA under the same transmit power.

2. The classical phased array

The core principle of conventional phased array relies on electromagnetic wave superposition. By phase coherence, it produces constructive interference to enhance beam intensity in a target direction, while simultaneously generating destructive interference to suppress signals elsewhere. This phased control

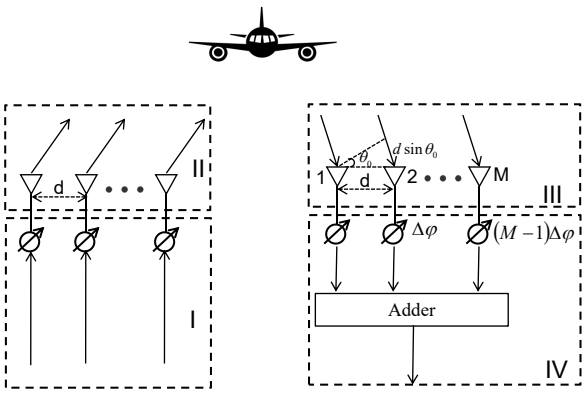


Fig. 1. Schematic diagram of the classical phased array. The total process is divided into four stages. Step I: Signal generation, after the signal is generated by each phase shifter, it is controlled by the initial phase. Step II: Signal transmission, the modulated signal is transmitted through each antenna and interfered with in free space. Step III: Signal reception, each antenna receives signals from the far field. Step IV: Signal processing and detection, the signal received by each antenna first passes through a phase shifter and then enters an adder for beamforming.

mechanism enables rapid electronic beam steering and high-gain beamforming, essential for multi-target tracking and adaptive spatial signal processing.

Fig. 1 illustrates the schematic of a one-dimensional linear phased array. This system employs phase shifting across array elements to control beam direction: each radiating element is connected to a phase shifter, which adjusts the relative phase distribution. Consequently, the electromagnetic wavefront of the array is reconfigured, achieving beam scanning. Assuming the linear array's axis is oriented at 0°, with element spacing d, and considering the far-field condition (where each antenna element transmits/receives signals in the same direction), let the incident angle be θ_0. The wave path difference between two adjacent antenna elements is given by:

$$\Delta\varphi_0 = kd\sin\theta_0. \tag{1}$$

Here, $k = 2\pi/\lambda$, which is the wave number, and λ is the wavelength of the signal. Therefore, the phase difference between any two antenna elements is:

$$\Delta\varphi_0 = \frac{2\pi d}{\lambda} \cdot \sin\theta_0. \tag{2}$$

This is also the relationship between the beam steering angle in a uniform linear antenna array and the phase shift of each antenna element's phase shifter. By adjusting the phase shifters of adjacent array elements, the beam can be steered to a target direction for signal transmission or reception. The electromagnetic field after interference at the target point or the electromagnetic field entering the adder can be expressed as:

$$E(\theta) = \sum_{m=0}^{M-1} A_m e^{im(kd\sin\theta_0 - \Delta\varphi)}, \tag{3}$$

where A_m is the amplitude, k is the wave number, θ_0 is the angle at which the target is located, and $\Delta\varphi = kd\sin\theta$ is the phase difference between two neighbouring unit phase shifters. When $\theta = \theta_0$, this yields the maximum value of the antenna pattern. Thus, varying the phase difference $\Delta\varphi$ between adjacent antennas in the linear array allows us to adjust the direction of the array beam's maximum, which refers to the direction θ.

3. Quantum-enhanced phased array

3.1. Preparation and practical constraints of multi-mode NOON states

Before presenting the quantum phased array model, we briefly describe the preparation of the M-mode N-photon NOON state used as the entangled resource in our scheme. Various methods for preparing NOON states have been discussed in the literature [31–33]. Among them, Ref. [33] presents a scheme in which multi-mode NOON states are generated from a fixed-total-photon-number input state with the assistance of Fock-state filters. In this scheme, a deterministic N-photon Fock state is distributed into M optical modes by a splitter network with phase compensation, producing a fixed-total-photon-number multi-mode state. A cascade of Fock-state filters (FSFs) [34] is then used to conditionally remove the components in which photons are distributed among multiple modes. As a result, only the terms where all N photons occupy a single mode remain, yielding the target M-mode N-photon NOON state

$$|\Psi\rangle = \frac{1}{\sqrt{M}} \left(|N, 0, \cdots, 0\rangle + |0, N, \cdots, 0\rangle + \cdots + |0, \cdots, 0, N\rangle \right). \tag{4}$$

Although the above preparation scheme can, in principle, be extended to larger photon and mode numbers, the complexity of the required optical network increases rapidly with both M and N. Conditional filtering, photon loss, and imperfect interference further reduce the generation efficiency and state fidelity. Consequently, current experimental realizations of multimode NOON states remain largely limited to the few-photon and few-mode regime [29].

Maintaining multimode coherence also requires stable relative phases among all optical paths. For a small number of paths, active stabilization can be implemented using auxiliary locking fields and feedback control [35]. For networked fiber links, classical stabilization channels can be used to stabilize individual links and distribute a common phase reference [36]. Extending these techniques to a large array would require a scalable multi-path phase-control architecture, with increasingly stringent stability requirements as M and N increase.

Despite these practical limitations, the multimode NOON state provides a well-defined multiphoton phase response and enables analytical beamforming expressions in terms of M and N. It therefore serves as a suitable theoretical benchmark for demonstrating the operating principle of multiphoton spatial beamforming. Given the proof-of-principle theoretical scope of this work, the following analysis assumes ideal preparation, distribution, and phase stabilization of the multimode NOON state.

3.2. Quantum-enhanced phased array

In this section, we model the quantum phased array by analogy to the classical phased array. Fig. 2 illustrates the quantum phased array setup (M-mode N-photon NOON state case). We establish a one-to-one correspondence with the classical phased array's operational process, indicating that the corresponding quantum phased array model can likewise be decomposed into four distinct stages.

Step I: The M-mode N-photon NOON state prepared above (Eq. (4)) is distributed into the M transmission paths of the array, with the j-th mode routed to the j-th path. Photonic phase shifters φ_j ($j = 1, 2, \cdots, M$) are then integrated into the corresponding optical paths to modulate the phase of each mode before transmission. This mode-dependent phase modulation controls the spatial emission direction of the quantum phased array and enables beam scanning.

Step II The quantum coherent superposition (QCS) describes the quantum interference occurring in free space, and its fundamental physical mechanism can be analogized to Young's double-slit interference

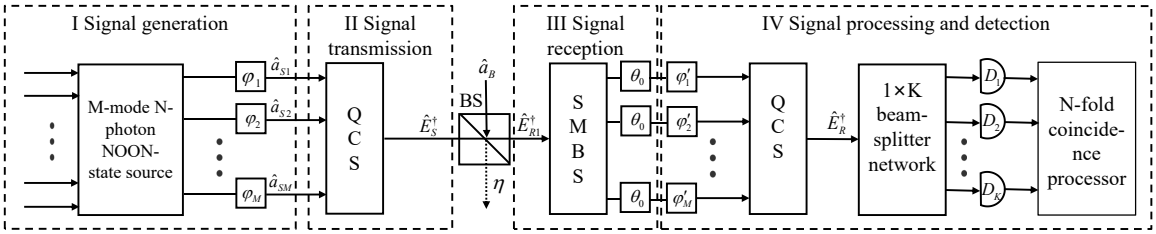


Fig. 2. The schematic of quantum phased array design. φ_j and φ'_j $(j = 1, 2, \cdots, M)$ represent the photonic phase shifters in the transmission and reception paths, respectively. The symbol θ_0 denotes the target angle, indicating that the signals received by each antenna originate from the direction of θ_0. The first QCS corresponds to the quantum interference of the transmitted signal at the target, whereas the second QCS refers to the quantum coherent superposition of the received signals after phase compensation. D_1-D_K denote the single-photon detectors used for N-fold coincidence detection.

—where each slit is analogous to an antenna in a quantum phased array. Once the quantum states are generated, each antenna emits them into free space. The emitted quantum states subsequently interfere in free space, and the direction of maximum intensity in the resulting interference pattern corresponds to the beam steering direction of the quantum phased array. Thus, the mathematical model of this QCS is expressed as:

$$\hat{E}_S^+ = \sum_{m=1}^{M} \hat{a}_{Sm} e^{i(m-1)\Delta\varphi_0} \, (m = 1, 2, \cdots M) \,, \tag{5}$$

where $\hat{a}_{Sm}$ denotes the annihilation operator for each antenna mode. These operators obey the standard photon commutation relations: $[\hat{a}_{Sm}, \hat{a}^\dagger_{Sn}] = \delta_{mn}$. $\Delta\varphi_0 = \varphi_{m+1} - \varphi_m = kd \sin\theta_0$ denotes the phase difference induced by the path difference between adjacent antennas. Here, d is the spacing between the antennas, θ_0 is the angle of the point target, and $k = 2\pi/\lambda$ (where λ denotes the optical wavelength).

Step III The quantum beam splitter (BS) model is used to model the noisy and lossy channel, the output field operator can be described as:

$$\hat{E}_{R1}^+ = \sum_{m=1}^{M} \hat{b}_m e^{i(m-1)\Delta\varphi_0}, \tag{6}$$

where $\hat{b}_m = \sqrt{\eta}\hat{a}_{Sm} + \sqrt{1-\eta}\hat{a}_{Bm}$, $\hat{a}_{Bm}$ denotes the annihilation operator for the noise photon mode, and η denotes the total transmissivity. In realistic radar scenarios, thermal noise arises during both forward signal propagation from the transmitter to the target and the subsequent return path to the receiver. Following the established model in quantum illumination [37–39], we assume identical noise temperatures for both paths. This allows the entire process to be effectively described by a single thermal noise field, as shown in Fig. 2.

The signal reception at an angle θ_0 by the M antennas is modeled by a single-input multiple-output beam splitter (SMBS). This model splits a single input mode into M output channels, thereby distributing the received signal across the M output paths.

Step IV After the transmitted quantum signal is reflected by the target, it is received by each antenna as a planar wavefront. Due to differences in the propagation path to each antenna, phase variations arise among the received signals. A photon phase shifter φ'_j is placed after each receiving antenna to compensate for these phase differences. By setting appropriate values for the M phase shifters, the signal from the scanning angle θ can be enhanced. Specifically, the phase shifters modulate the phase of the incident signal

from the target direction to compensate for the optical phase discrepancies, thereby enabling quantum coherent superposition.

For a uniform linear array, the phase shift factor applied to the m-th antenna is $e^{-im\Delta\varphi}(m = 2,3,\cdots M)$, where $\Delta\varphi = kd\sin\theta = 2\pi d\sin\theta/\lambda$, and λ is the optical wavelength. Once phase compensation is applied to each received signal, quantum coherent superposition is performed. The objective of this QCS process is to concentrate the signal energy from direction θ_0 into the output, corresponding to the adder module shown in Step IV of Fig. 1. Defining the phase difference as $\Delta\phi = \Delta\varphi_0 - \Delta\varphi = kd(\sin\theta_0 - \sin\theta)$, the output field operator can be expressed as:

$$\hat{E}_R^+ = \sum_{m=1}^{M} \hat{b}_m e^{i(m-1)\Delta\phi}. \tag{7}$$

Finally, the selected output mode obtained after quantum coherent superposition is split into K channels by a $1 \times K$ beam-splitter network and detected by K single-photon detectors $D_1 - D_K$. Here, $K \geq N$ provides at least N output channels, allowing an N-photon event to produce detection clicks in N distinct detectors. Detection events occurring at N detectors within the same coincidence window are identified and recorded by the coincidence-processing unit as an N-fold coincidence event. This coincidence-detection scheme has been experimentally demonstrated for multimode NOON states [29]. By varying the steering angle, the measured N-fold coincidence rate yields the Nth-order directional response of the NPA. The next section provides a detailed analysis of beamforing in the N-photon entangled states and coherent states.

4. Quantum phased array beamforming

4.1. The CPA beamforming

First, we consider the scenario in which the signal emitted by the quantum phased array consists of classical light with an average photon number of N. This corresponds to the case where M receiving antennas receive coherent states incident from the direction θ_0. Let $|\alpha\rangle$ denote a coherent state with an average photon number of N, written as the tensor product $|\alpha\rangle = |\alpha_1\rangle|\alpha_2\rangle\cdots|\alpha_M\rangle$, where each mode $|\alpha_m\rangle$ is generated by independent and identical laser sources.

$$|\alpha_m\rangle = e^{-\frac{|\alpha|^2}{2}} \sum_{n=0}^{\infty} \frac{\alpha^n}{\sqrt{n!}} \left(\hat{a}^\dagger\right)^n |0\rangle . \tag{8}$$

For the coherent state $|\alpha_m\rangle$, the eigenvalue equation $\hat{a}|\alpha_m\rangle = \alpha_m|\alpha_m\rangle$ holds, where α_m is the eigenvalue of the annihilation operator $\hat{a}$ acting on the eigenstate $|\alpha_m\rangle$. The average photon number per antenna is given by $\langle\alpha_m|\hat{a}^\dagger\hat{a}|\alpha_m\rangle = |\alpha_m|^2 = \frac{N}{M}$. Then the field operator at the detection point x is:

$$\begin{aligned} \hat{E}_S^+(x) &= \hat{a}_{S1} + \hat{a}_{S2}e^{i\Delta\phi} + \cdots + \hat{a}_{SM}e^{i(M-1)\Delta\phi} \\ \hat{E}_S^-(x) &= \left[\hat{E}_S^+(x)\right]^\dagger \end{aligned} . \tag{9}$$

Here, $\hat{a}_{Sm}\,(m = 1,2,\cdots,M)$ represents the annihilation operator of the signal photons on each antenna mode. $\Delta\phi = \Delta\varphi_0 - \Delta\varphi = kd(\sin\theta_0 - \sin\theta)$, $\Delta\varphi_0$ denotes the phase difference caused by the path difference of the target signal arriving at different array elements, and $\Delta\varphi$ denotes the phase difference compensated by the photonic phase shifters for enhancing the signal in the target direction.

For a CPA, the optical fields emitted by different array elements possess well-defined relative phases and interfere coherently at the field-amplitude level, following the same beamforming principle as a classical phased array. The resulting directional beam is therefore formed through first-order interelement interference and is characterized by the first-order correlation function

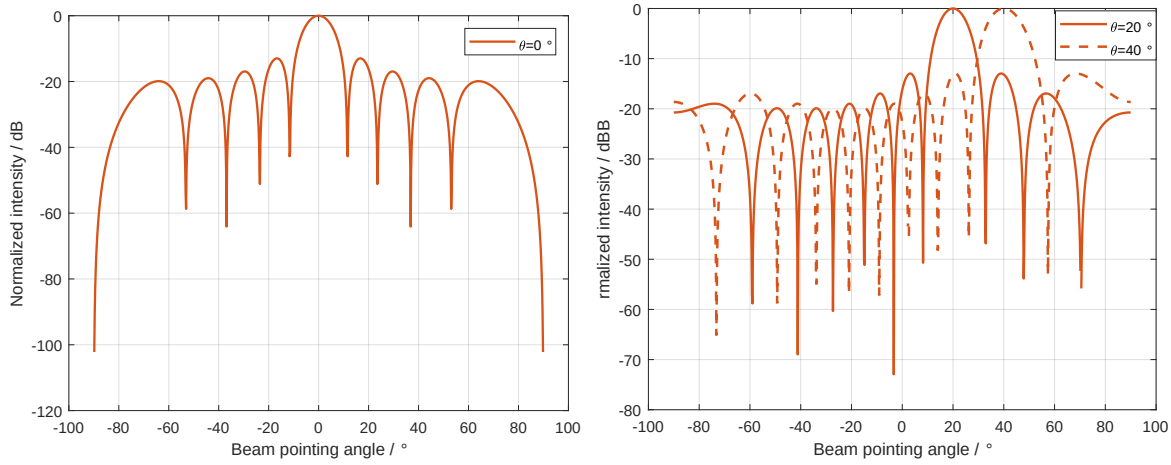
$$I_c = \langle\alpha| \hat{E}_S^- (x) \hat{E}_S^+ (x) |\alpha\rangle = \frac{N}{M} \left(M + 2 \sum_{m=1}^{M-1} m \cos (M-m) \Delta\phi \right). \tag{10}$$

This quantity gives the average optical-intensity distribution in space and therefore directly represents the beam pattern of the CPA. The Nth-order correlation function can also be calculated or measured for the coherent output field. However, the normally ordered Nth-order correlation of a coherent state factorizes into products of first-order correlations. Consequently, the resulting Nth-order coincidence response describes only the multiphoton detection statistics of the already formed first-order beam and does not constitute the beamforming result of the CPA [40].

When the array receives a signal from an angle θ_0, the antenna pattern reaches its maximum value at $\theta = \theta_0$. Thus, the pointing angle θ of the array beam must satisfy:

$$\theta = arc\sin \left(\frac{\lambda}{2\pi d} \Delta\varphi \right) = \theta_0. \tag{11}$$

Fig. 3 shows the radiation pattern of the CPA when the number of array elements $M = 10$, the number of photons emitted $N = 4$, and the array element spacing $d = \lambda/2$. Specifically, Fig. 3(a) illustrates the radiation pattern when the beam is steered to the normal direction ($\theta = 0°$). By varying the inter-element phase shift $\Delta\varphi$, the beam direction can be flexibly adjusted. Fig. 3(b) shows the radiation patterns for beam pointing angles of $\theta = 20°$ and $\theta = 40°$, respectively. This result highlights a key advantage of phased array—flexible and rapid beam steering without physical movement.



(a) (b)

Fig. 3. The patterns of the CPA, where the number of array antenna elements $M = 10$, the number of photons emitted $N = 4$, and the spacing between the array elements is $\lambda/2$. (a) The CPA pattern with a beam pointing angle $\theta = 0°$. (b) The CPA pattern with beam pointing angle $\theta = 20°$ and $\theta = 40°$.

4.2. The NPA beamforming

Next, we consider the case of a quantum phased array employing an entangled state. As illustrated in Fig. 2, under ideal conditions with no noise or losses and when the transmitted signal is prepared in

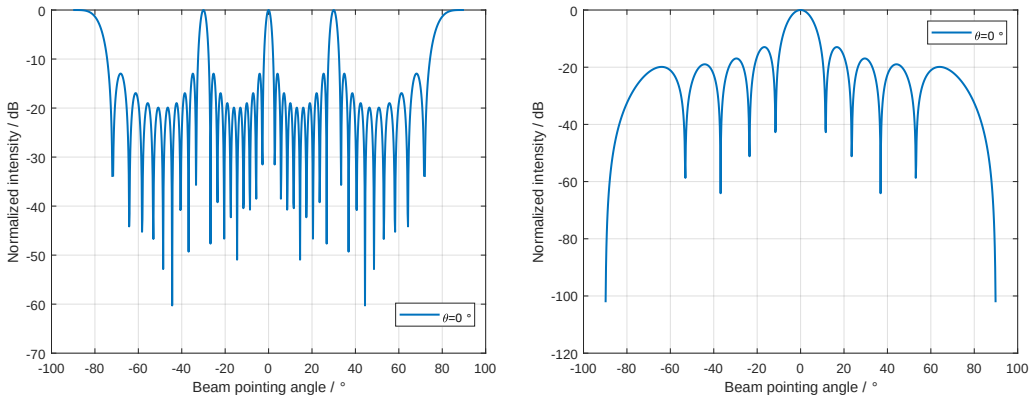
a NOON state, the receiving antenna array receives an M-mode N-photon NOON state $|\Psi\rangle$ from the angle θ_0.

Unlike the CPA, whose beamforming is governed by first-order field interference and average intensity measurements, the quantum coherence of a NOON-state signal is manifested through Nth-order quantum interference. Therefore, the beamforming pattern of the NPA is obtained from the Nth-order correlation measurement, corresponding to the coincidence response of N photons. The corresponding Nth-order correlation function is calculated as

$$I_q = Tr\left[\hat{\rho}\hat{E}_S^-(x)\cdots\hat{E}_S^-(x)\,\hat{E}_S^+(x)\cdots\hat{E}_S^+(x)\right] = N! + 2\frac{N!}{M}\sum_{m=1}^{M-1}(M-m)\cos(mN\Delta\phi). \tag{12}$$

Fig. 4 shows the Nth-order correlation pattern of the NPA for $M = 10$, $N = 4$, and a beam pointing angle of $\theta = 0°$. Similar to the CPA case in Fig. 3, the directional maximum of the NPA pattern can be steered by adjusting the phase difference between adjacent antennas. For the NPA, the main lobe represents the direction of maximum intensity correlation, or equivalently the strongest coincidence response, while grating lobes correspond to undesired coincidence peaks away from the target direction.

As shown in Fig. 4(a), when the NPA element spacing is $d = \lambda/2$, the main lobe becomes narrower than that of the CPA in Fig. 3(a), but additional grating lobes appear. In contrast, when the spacing is reduced to $d = \lambda/8$, as shown in Fig. 4(b), the grating lobes are eliminated and the normalized NPA pattern has the same shape as the normalized CPA intensity pattern in Fig. 3(a). More generally, for an N-photon NOON state, choosing $d = \lambda/(2N)$ makes the normalized NPA pattern identical in shape to that of the CPA with $d = \lambda/2$. This behavior originates from the phase super-resolution effect of N-photon entangled states, where the Nth-order interference depends on the accumulated phase $N\Delta\phi$ [28–30].



(a) (b)

Fig. 4. The patterns of the NPA, where the number of array antenna elements $M = 10$, the number of photons emitted $N = 4$, and the beam pointing angle $\theta = 0°$. (a) The NPA pattern with an array element spacing of $\lambda/2$. (b) The NPA pattern with an array element spacing of $\lambda/8$.

The comparison is performed under identical resource constraints, including the total average transmitted photon number and the number of array elements. The CPA and NPA are evaluated using the observables that directly characterize their respective beamforming responses, namely the average intensity for the CPA and the Nth-order intensity correlation for the NPA. Accordingly, the comparison focuses on the directional patterns generated by their distinct beamforming mechanisms under the same resource

constraints.

From a practical perspective, both photon loss and the finite preparation efficiency of the NOON state should be considered. We first consider the effect of uniform photon loss on beamforming. When all array elements experience the same transmissivity η, the normalized beam pattern remains unchanged because the loss introduces only an angle-independent attenuation factor. However, the beamforming signals are attenuated differently for the two schemes. Relative to the lossless case, the main-lobe peak satisfies $I_q^{\max}(\eta)/I_q^{\max}(1) = \eta^N$ for the NPA and $I_c^{\max}(\eta)/I_c^{\max}(1) = \eta$ for the CPA, where $I_q^{\max}$ and $I_c^{\max}$ denote the corresponding main-lobe peak values. Thus, the Nth-order beamforming signal of the NPA is more sensitive to photon loss than the first-order signal of the CPA.

Another practical factor is the finite preparation probability of the NOON state. Fig. 4 describes the normalized beam pattern conditioned on the successful preparation of the target NOON state. Therefore, the preparation probability does not change the normalized beam shape itself, but determines the number of useful NOON states available per unit time. Its effect on the SNR performance is discussed below.

5. SNR gain analysis of quantum phased arrays

5.1. The SNR gain analysis

The phased array enhances the target signal while suppressing interference through beam forming, thereby effectively improving the SNR. The following separately discusses the SNRs of the CPA and NPA. In the presence of noise and loss in the received signal, the photon annihilation operator at each receiving antenna is expressed as:

$$\hat{b}_m = \sqrt{\eta}\hat{a}_{Sm} + \sqrt{1-\eta}\hat{a}_{Bm}, (m = 1, 2, \cdots, M), \tag{13}$$

where $\hat{a}_{Sm}, \hat{a}_{Bm}$ denote the annihilation operators of the signal and noise at the m-th antenna and η is the total transmissivity.

In the case of the coherent state, the density operator of the echo received by the array is expressed as $\hat{\rho}_s = \hat{\rho}_c \otimes \hat{\rho}_B$, where $\hat{\rho}_c = |\alpha\rangle \langle\alpha|$ is the density operator of the coherent state with an average photon number of N_S and $\hat{\rho}_B$ represents the noise component. Consequently, the field operator at the detector can be written as:

$$\begin{aligned} \hat{E}_S^+(x) &= \hat{b}_1 + \hat{b}_2 e^{i\Delta\phi} + \cdots + \hat{b}_M e^{i(M-1)\Delta\phi} \\ \hat{E}_S^-(x) &= \left[\hat{E}_S^+(x)\right]^\dagger \end{aligned}. \tag{14}$$

The intensity distribution of the coherent state detected at point x is given by:

$$I_c = Tr\left[\hat{\rho}_c \otimes \hat{\rho}_B \hat{E}_S^-(x)\hat{E}_S^+(x)\right] = N_B + \eta\frac{N_S}{M}\left(M + 2\sum_{m=1}^{M-1} m\cos(M-m)\Delta\phi\right), \tag{15}$$

where N_S and N_B denote the total number of signal and noise photons received by the array, respectively. When the array antenna receives a signal from the target direction, each phase shifter adjusts the signal phase to align it with the phase required by the target direction, while simultaneously achieving precise compensation for the phase difference between array elements. At this point, the signals output by all array elements undergo in-phase coherent superposition, ultimately enabling the phased array to generate maximum output signal power. It is therefore necessary to set $\Delta\phi = \Delta\varphi_0 - \Delta\varphi = 0$, and the array's output SNR is defined as follows:

$$SNR_{(out)} = \frac{\eta\frac{N_S}{M}\left(M + 2\sum_{m=1}^{M-1} m\right)}{N_B} = \frac{\eta M N_S}{N_B}. \tag{16}$$

The number of input signal and noise photons per antenna are respectively:

$$\bar{N}_s = \eta N_S/M, \bar{N}_b = N_B/M. \tag{17}$$

The average input SNR for each antenna is

$$SNR_{(in)} = \frac{\bar{N}_s}{\bar{N}_b} = \frac{\eta N_S}{N_B}. \tag{18}$$

Thus, the SNR gain can be derived as

$$G_c = \mathrm{SNR}_{(\mathrm{out})}/\mathrm{SNR}_{(\mathrm{in})} = M. \tag{19}$$

In the case of an entangled state, when the echo received by the array is subject to noise and loss, the received quantum state can be described as a mixed state $\hat{\rho}_s = \hat{\rho}_q \otimes \hat{\rho}_B$, where $\hat{\rho}_q$ is the density operator of the NOON state and $\hat{\rho}_B$ represents the noise component. In the Heisenberg picture, the field operators evolve according to Eq. (14). For an N_S-photon multimode NOON state, N_S denotes the fixed total photon number and M denotes the number of spatial array modes. In each component, all N_S photons occupy one array mode, while the identity of the occupied mode is coherently superposed over the M possible paths. Accordingly, the correlation order is chosen as $N = N_S$, and the corresponding N_Sth-order correlation measurement of the received signal is expressed as:

$$\begin{aligned} I_q =& Tr\left[\hat{\rho}_q \otimes \hat{\rho}_B \hat{E}_S^-(x) \cdots \hat{E}_S^-(x)\, \hat{E}_S^+(x) \cdots \hat{E}_S^+(x)\right] \\ =& \eta^{N_S}\left(N_S! + \frac{2N_S!}{M}\sum_{m=1}^{M-1}(M-m)\cos(mN_S\Delta\phi)\right) + N_S!\sum_{j=0}^{N_S-1}\left(\frac{N_S!}{j!\,(N_S-j)!}\right)^2 \eta^j {N_B}^{N_S-j}. \end{aligned} \tag{20}$$

In quantum optics, the N_Sth-order coincidence count rate R_c is proportional to the N_Sth-order correlation function I_q [40,41]. Therefore, the output SNR of the NPA is defined as the ratio of the true coincidence count rate to the accidental coincidence count rate. The latter includes both the purely background-induced coincidence events and the mixed accidental coincidences caused by signal-background photons within the coincidence window:

$$\mathrm{SNR}_{(out)} = \frac{R_{N_S}\eta^{N_S}N_S!M}{N_S!(R_B)^{N_S}T_c^{N_S-1} + R_{N_S}\sum\limits_{j=1}^{N_S-1} N_S!\left[\frac{N_S!}{j!(N_S-j)!}\right]^2 \eta^j (R_B T_c)^{N_S-j}}. \tag{21}$$

Here, R_{N_S} denotes the emission rate of the N_S-photon NOON states. The quantity $N_B = Mn_BBT_{\mathrm{int}}$ is the total number of background photons accumulated over the integration time T_{int}, and $R_B = Mn_BB$ is the corresponding effective background count rate. Here, M is the number of antennas, B is the receiver bandwidth, and n_B is the average background photon number per electromagnetic spatiotemporal mode, calculated from the Planck thermal-noise formula. The coincidence-window width is denoted by T_c. Propagation loss, receiving coupling efficiency, and detector quantum efficiency are included in the total transmissivity η, while dark counts and other detector-related background events are included in R_B. The above expression gives the ensemble-averaged SNR determined by the mean true- and accidental-coincidence rates. For a finite integration time T_{int}, the measured coincidence counts exhibit Poisson statistical fluctuations. The simulations below assume a sufficiently long integration time such that enough coincidence events are accumulated and finite-count fluctuations remain small.

To simplify the notation, we define

$$X_B = N_S!(Mn_B B)^{N_S} T_c^{N_S-1} + R_{N_S} \sum_{j=1}^{N_S-1} N_S! \left[\frac{N_S!}{j!(N_S-j)!}\right]^2 \eta^j (Mn_B B T_c)^{N_S-j}. \tag{22}$$

Analogously, the input and output SNRs are derived as follows:

$$SNR_{(in)} = \eta \frac{N_S}{M} / \frac{N_B}{M} = \eta \frac{N_S}{N_B}, \tag{23}$$

$$SNR_{(out)} = \frac{R_{N_S} \eta^{N_S} N_S! M}{X_B}. \tag{24}$$

The resulting SNR gain of the NPA is obtained as:

$$G_q = SNR_{(out)}/SNR_{(in)} = \frac{R_{N_S} \eta^{N_S-1} (N_S-1)! M N_B}{X_B}. \tag{25}$$

To account for the finite preparation efficiency, we define P_{p} as the probability of successfully preparing the target NOON state in each preparation trial. The corresponding NOON state emission rate is written as

$$R_{N_S} = P_{\mathrm{p}} R_{\mathrm{t}}, \tag{26}$$

where R_{t} is the preparation trial rate. Fig. 5 presents the variation of the SNR gain for both CPA (G_c, from Eq. (19)) and NPA (G_q, from Eq. (25)) with respect to different parameters. In Fig. 5(a), the SNR gain is plotted against the number of antennas M for $N_S = 2$ and $N_S = 3$. G_c exhibits a gradual increase with M, whereas G_q remains nearly constant for $N_S = 2$ and even decreases for $N_S = 3$. This behavior occurs because, in higher-order correlation measurements ($N_S > 2$), increasing M amplifies the relative contribution of noise in the NPA scheme, thereby reducing its SNR gain.

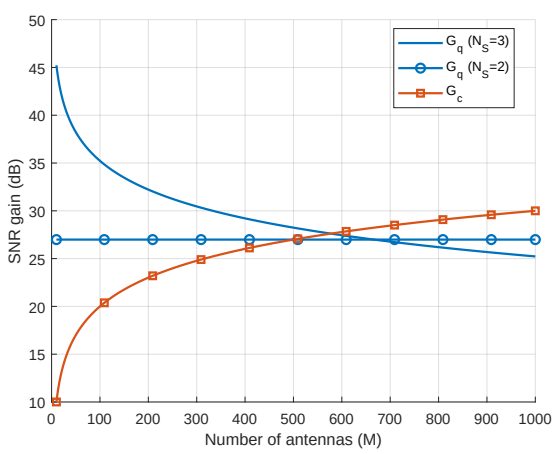
Fig. 5(b) shows that G_c remains unchanged with increasing N_S, while G_q grows exponentially. For $N_S > 2$, the NPA can achieve significantly higher SNR gains than the CPA. Fig. 5(c) and 5(d) illustrate that G_q decreases with increasing N_B and increases with increasing η, respectively. Fig. 5(e) further shows the dependence of G_q on P_{p}. As P_{p} increases, the effective NOON-state emission rate increases, resulting in a higher SNR gain.

It is noteworthy that the NPA and CPA exhibit a significant difference in SNR gain. For the CPA, the gain exhibits a simple linear positive correlation with the number of antennas, which is consistent with the classical characteristic of SNR gain for classical phased arrays. In contrast, the gain of the NPA depends on multiple parameters, including M, N_S, η, and N_B. Since the SNR gain of the NPA is not solely determined by M, it offers several quantum advantages over the CPA in enhancing SNR performance. For instance, under ideal conditions, the NPA can achieve the same SNR gain as the CPA with fewer antennas, highlighting its potential advantage for system miniaturization. (as shown in Fig. 5(a)). Moreover, the SNR gain of the NPA can be further increased by raising the signal photon number N_S (Fig. 5(b)), reducing the noise photon number N_B (Fig. 5(c)), or improving the transmissivity η (Fig. 5(d)).

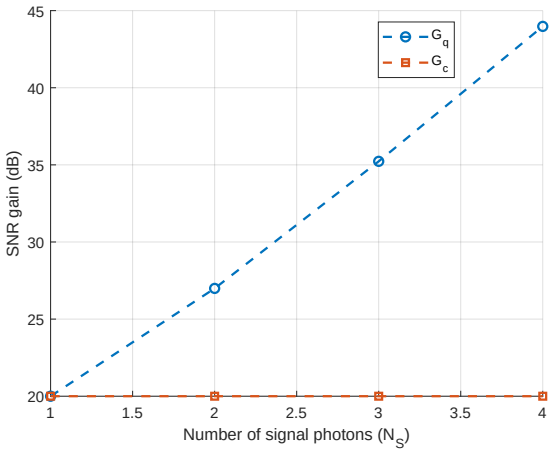
5.2. The maximum detection range

Based on the above-derived SNR gain, we investigate the maximum detection range of the NPA relative to the CPA in specific detection scenarios by introducing the radar equation (lidar equation for the optical band), which is expressed as [42]:

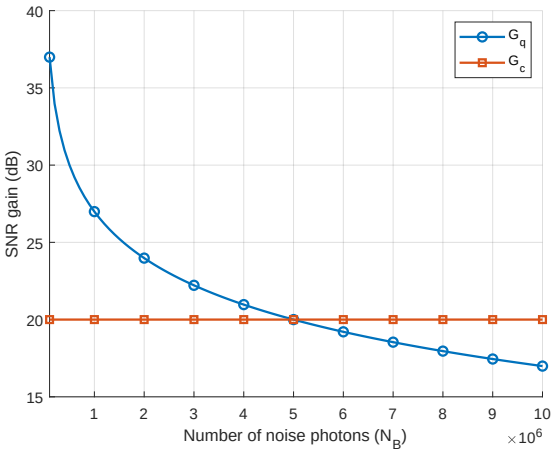
$$P_r = \frac{P_t A_r \sigma \eta \eta_{sys}}{4\pi R^2}. \tag{27}$$



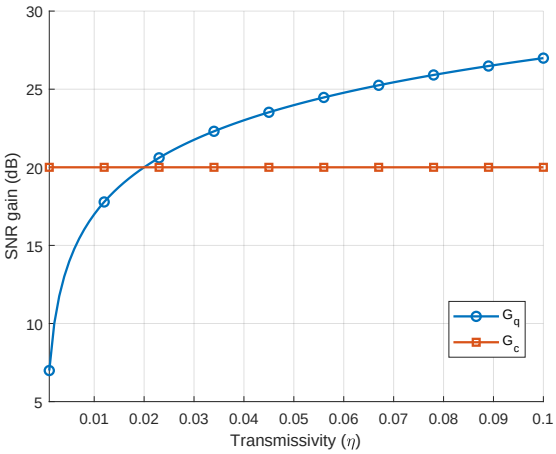
(a)



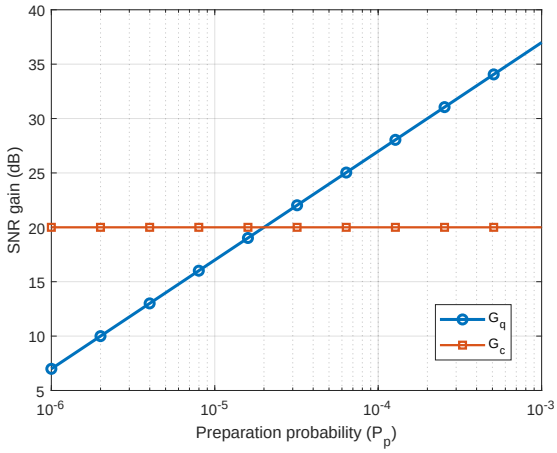
(b)



(c)



(d)



(e)

Fig. 5. Variation of the SNR gain for the NPA (G_q) and the CPA (G_c) with different parameters. (a) G_q and G_c versus M, where M ranges from 10 to 10^3. (b)–(e) Variations with N_S, N_B, η, and P_p, respectively. The simulation parameters are $T_c = 10^{-8}\,\mathrm{s}$, $\eta = 0.1$, $T_\mathrm{int} = 1\,\mathrm{s}$, $N_S = 2$, $M = 10^2$, $n_B = 10^{-4}$, $B \approx 1/T_c$, and $N_B = Mn_BBT_\mathrm{int}$. For Figs. 5(a)–5(d), $R_{N_S} = 1$. For Fig. 5(e), $R_{N_S} = P_\mathrm{p}R_\mathrm{t}$ with $R_\mathrm{t} = 10^4\,\mathrm{s}^{-1}$.

In this equation, the transmissivity is given by $\eta = e^{-KL} = e^{-2KR}$, where K is the attenuation coefficient and $L = 2R$ is the round-trip propagation distance through the lossy medium, with R being the one-way detection range. The received and transmitted signal powers, P_r and P_t, are expressed in photon-number units. The transmitted signal has an average photon number of N_S, i.e., $P_t = N_S$. Additionally, σ denotes the target reflectivity, and η_{sys} denotes the optical system transmission efficiency, and A_r is the effective aperture area of the receiving array.

According to Eq. (27), the received powers of the CPA and NPA are identical and can be written as the unified formula below:

$$P_r^c = P_r^q = \frac{N_S M \lambda^2 \sigma \eta \eta_{sys}}{(4\pi)^2 R^2}, \tag{28}$$

The noise power received by both arrays is given as:

$$P_n^c = P_n^q = N_B, \tag{29}$$

Therefore, in specific radar detection scenarios with full-link power loss, the input SNR for both architectures is calculated as:

$$SNR_{(in)}^c = SNR_{(in)}^q = \frac{N_S M \lambda^2 \sigma \eta \eta_{sys}}{(4\pi)^2 R^2 N_B}, \tag{30}$$

It should be noted that Eqs. (18), (23), and (30) all describe the input SNR of the array. Their essential difference lies in how the received signal power is modeled. In Eqs. (18) and (23), the received power is taken as $P_r = \eta N_S$, reflecting only the link attenuation. In contrast, Eq. (30) derives the received power from the lidar equation (Eq. (27)), which represents a more complete physical model incorporating the full round-trip signal path—transmission, target reflection, and reception.

Next, using the SNR gains of the CPA and NPA from Eqs. (19) and (25), the output SNR in the radar detection scenario is computed as follows:

$$SNR_{(out)}^c = G_c SNR_{(in)}^c = \frac{N_S M^2 \lambda^2 \sigma \eta \eta_{sys}}{(4\pi)^2 R^2 N_B}, \tag{31}$$

$$SNR_{(out)}^q = G_q SNR_{(in)}^q = \frac{\lambda^2 M^2 \sigma \eta_{sys} \eta^{N_S} N_S \, (N_S - 1)!}{(4\pi)^2 R^2 X_B}. \tag{32}$$

The simulation parameters are listed in Table 1. For $\lambda = 2\,\mu$m and room temperature ($T = 300\,$K), the atmospheric attenuation coefficient is taken as $K = 0.1\,\text{dB/km} = 0.023\,\text{km}^{-1}$. Based on the previously calculated thermal noise photon number, the total number of noise photons received by the array is $N_B \approx 10^{-2} \times M$. The minimum detectable SNR ($\text{SNR}_{\min}$) is defined as the threshold output SNR required for reliable target detection after array signal processing. The maximum detection range, $R_{\max}$, is defined as the distance at which the actual SNR equals $\text{SNR}_{\min}$ in Eqs. (31) and (32).

Fig. 6 shows that the output SNRs of both the NPA and CPA decrease monotonically with increasing detection range. For a prescribed $SNR_{\min} = 13$ dB, the corresponding maximum detection ranges are approximately $R_{\max}^q \approx 3.02$ cm for the NPA and $R_{\max}^c \approx 0.04$ cm for the CPA. These results show that, under the same average photon-number condition, the NPA provides a longer detection range than the CPA. It should be noted that the relatively small photon number used in the simulation leads to small absolute detection ranges for both schemes. To enable the comparison shown in Fig. 6, a large number of array elements M is used to ensure that both the CPA and the NPA exceed the prescribed detection

Table 1. Simulation parameters. λ represents the wavelength of the transmitted signal, σ is the target reflectivity, N_S is the total number of signal photons, M is the number of antennas, K is the attenuation coefficient, η_{sys} is the transmission efficiency of the optical system, $SNR_{\min}$ is the minimum detectable SNR, and N_B is the total number of noise photons.

$\lambda(\mu m)$	σ	N_S	M	$K(\mathrm{m}^{-1})$	η_{sys}	$SNR_{\min}(\mathrm{dB})$	N_B
2	0.9	2	10^6	0.023×10^{-3}	0.8	13	$10^{-2} \times M$

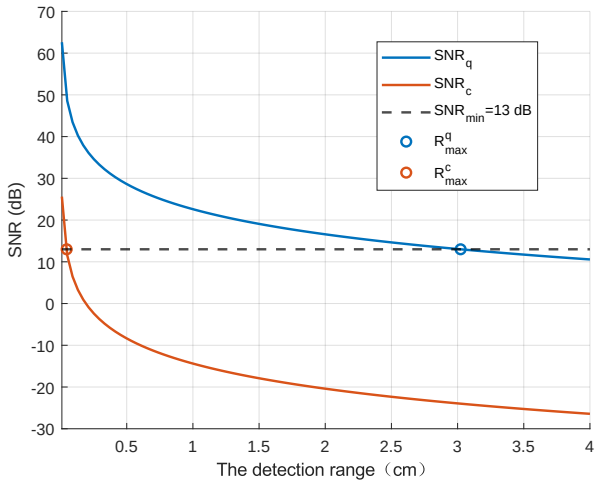


Fig. 6. Variation of NPA and CPA output SNR with detection range. The intersection points $R^q_{\max}$ and $R^c_{\max}$ represent the maximum detection ranges of the NPA and CPA, respectively.

threshold. The results should therefore be regarded as a theoretical illustration of the relative advantage of the NPA rather than as a prediction of practical array size or radar performance.

6. Conclusion

In summary, by analogy with the conventional phased-array model, this work proposes a quantum-enhanced phased-array architecture. Within this framework, we first calculate the beamforming of the NPA and CPA. Our analysis demonstrates that the NPA reduces the required array aperture by a factor of N relative to the CPA while generating identical normalized beams with the same shape. Subsequently, we quantify the SNR gains of the NPA and the CPA separately, and analyze the effects of different parameters on them. The result shows that under certain parameter conditions, the NPA can achieve a higher SNR gain than the CPA. Finally, by incorporating radar equations, we demonstrate that the NPA is able to detect longer ranges than the CPA at identical transmit power levels.

It should be emphasized that all results presented in this work constitute a theoretical proof-of-principle analysis under idealized conditions. The well-defined multiphoton interference characteristics of the multimode NOON state allow closed-form beamforming expressions to be derived for arbitrary photon number N and array-element number M. It therefore serves as a suitable benchmark for demonstrating the core principle of quantum-enhanced phased-array beamforming, despite its sensitivity to loss and imperfections [43]. The proposed framework is not restricted to multimode NOON states and can be extended to other quantum resources, as illustrated by the two-element TMSV-based example presented

in the Appendix A.

Appendix A: TMSV-state beamforming in a quantum phased array

Among the alternative quantum resources that can be incorporated into this framework, squeezed states and continuous variable Gaussian entangled states have a well-established experimental basis in state preparation and phase control. Zheng et al. have experimentally demonstrated squeezed vacuum states and continuous variable entangled states with precise phase control [44,45]. These quantum resources have further been applied to squeezing enhanced radio frequency signal sensing and distributed quantum positioning and ranging [23,24]. These experimental advances motivate the consideration of Gaussian entangled states as promising resources for future implementations of quantum phased arrays.

For a general M-element quantum phased array based on Gaussian entangled states, the beamforming behavior depends on the complete multimode covariance matrix and the linear optical network used to distribute the quantum correlations. Since a closed-form beamforming expression for an arbitrary number of modes is generally difficult to obtain, we consider a TMSV state in a two-element array as a representative example. The TMSV state is written as

$$|\xi\rangle = \frac{1}{\cosh r}\sum_{n=0}^{\infty}(-1)^n e^{in\vartheta}(\tanh r)^n|n,n\rangle. \tag{33}$$

As shown in Fig. 7, its two modes are mixed by a balanced beam splitter and transmitted through two phase-controlled array elements. The mode operators incident on the two transmitting elements are

$$\hat{a}_{S1} = \frac{\hat{a}_1 + \hat{a}_2}{\sqrt{2}}, \qquad \hat{a}_{S2} = \frac{-\hat{a}_1 + \hat{a}_2}{\sqrt{2}}. \tag{34}$$

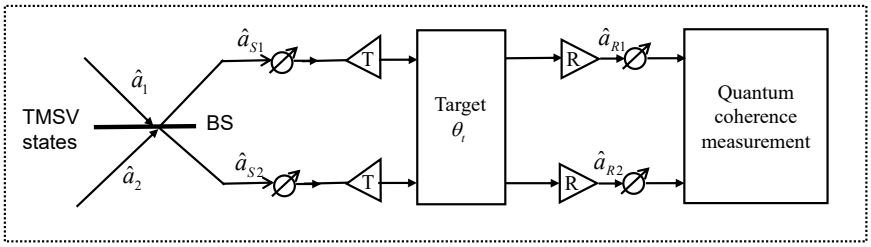


Fig. 7. Schematic of the two-element TMSV-state quantum phased array.

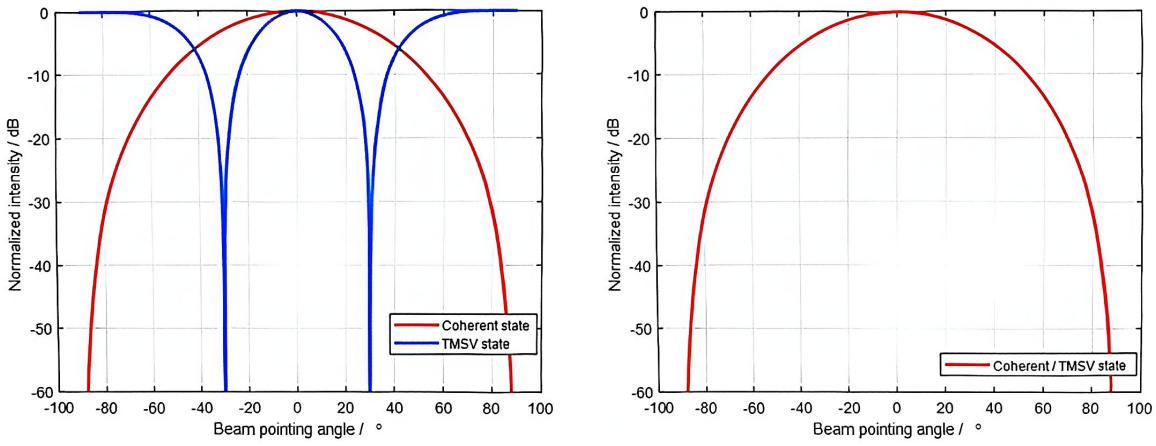
After phase compensation, with the fixed phase bias included in $\Delta\phi$, the output field is expressed as

$$\hat{E}_R^+ = \hat{a}_{S1} + e^{i\Delta\phi}\hat{a}_{S2}. \tag{35}$$

The corresponding second-order detection response is

$$\begin{aligned} G^{(2)} &= \langle\xi|\,\hat{E}_R^-\hat{E}_R^-\hat{E}_R^+\hat{E}_R^+\,|\xi\rangle \\ &= 8\bar{N}_S^2 + 4\bar{N}_S\left(1+\bar{N}_S\right)\sin^2\Delta\phi, \end{aligned} \tag{36}$$

where $\bar{N}_S = \sinh^2 r$ is the average photon number in each TMSV mode. This result demonstrates that the phase-sensitive second-order correlations originating from the TMSV resource can produce a directional response.



(a) (b)

Fig. 8. Normalized directional responses of the coherent-state and TMSV-derived two-element arrays for different interelement spacings. (a) Both arrays have $d = \lambda/2$. (b) The coherent-state array has $d = \lambda/2$, whereas the TMSV-derived array has $d = \lambda/4$.

As shown in Fig. 8, for the same spacing $d = \lambda/2$, the TMSV-derived array exhibits a narrower main lobe than the coherent-state array, accompanied by additional side peaks. When its spacing is reduced to $d = \lambda/4$, it has the same normalized beam pattern as the coherent-state array with $d = \lambda/2$. This result demonstrates that the TMSV-derived array can reproduce the normalized beam pattern of the coherent-state array with half the element spacing, thereby reducing the physical aperture required to achieve the same directional response.

Acknowledgment

This work was supported by the National Natural Science Foundation of China under Grant (No.62571392).

References

[1] Einstein A, Podolsky B and Rosen N 1935 *Phys. Rev.* **47** 777
[2] Zhang Z S and Zhuang Q T 2021 *Quantum Sci. Technol.* **6** 043001
[3] Bennett C H and DiVincenzo D P 2000 *Nature* **404** 247
[4] Braunstein S L and van Loock P 2005 *Rev. Mod. Phys.* **77** 513
[5] Weedbrook C, Pirandola S, García-Patrón R, Cerf N J, Ralph T C, Shapiro J H and Lloyd S 2012 *Rev. Mod. Phys.* **84** 621
[6] Gisin N and Thew R 2007 *Nat. Photonics* **1** 165
[7] Cho C H, Chen C Y, Chen K C, Huang T W, Hsu M C, Cao N P, Zeng B, Tan S G and Chang C R 2021 *Chinese J. Phys.* **72** 248
[8] Lloyd S 2008 *Science* **321** 1463
[9] Wasilousky P A, Smith K H, Glasser R, Burdge G L and others 2011 *Proc. SPIE* **8163** 816305
[10] Lee S Y, Ihn Y S and Kim Z 2021 *Phys. Rev. A* **103** 012411
[11] Hao S H, Shi H W, Gagatsos C N, Mishra M, Bash B, Djordjevic I, Guha S, Zhuang Q T and Zhang Z S 2022 *Phys. Rev. Lett.* **129** 010501
[12] Assouly R, Dassonneville R, Peronnin T, Bienfait A and Huard B 2023 *Nat. Phys.* **19** 1418
[13] Duan H, Li J, Wang W H, Guo J H and Guo Q H 2026 *IEEE Trans. Aerosp. Electron. Syst.* **62** 11755
[14] Zhang Z S, Mouradian S, Wong F N C and Shapiro J H 2015 *Phys. Rev. Lett.* **114** 110506
[15] Wei R Y, Li J, Wang W H, Meng S H, Zhang B S and Guo Q H 2022 *Opt. Express* **30** 36167
[16] Karsa A, Fletcher A, Spedalieri G and Pirandola S 2024 *Rep. Prog. Phys.* **87** 094001
[17] Gallego Torromé R and Barzanjeh S 2024 *Prog. Quantum Electron.* **93** 100497

[18] Luong D, Rajan S and Balaji B 2019 *2019 IEEE International Symposium on Phased Array System & Technology (PAST)* 1
[19] Wang W H, Li J, Wei R Y, Guo J H and Guo Q H 2024 *Opt. Lett.* **49** 5459
[20] Zhao X B, Zhang Z S and Zhuang Q T 2025 *Commun. Phys.* **8** 54
[21] Xia Y, Li W, Clark W, Hart D, Zhuang Q and Zhang Z 2020 *Phys. Rev. Lett.* **124** 150502
[22] Xia Y, Li W, Zhuang Q and Zhang Z 2021 *Phys. Rev. X* **11** 021047
[23] Sun X C, Li W, Tian Y H, Li F, Tian L, Wang Y J and Zheng Y H 2022 *Photon. Res.* **10** 2886
[24] Li W, Ju M J, Li Q H, Li R X, Yao W X, Wu Y M, Wang Y J, Tian L, Shi S P and Zheng Y H 2024 *Chin. Opt. Lett.* **22** 072701
[25] Li W, Li Q H, Wang Y F, Wang Y J, Tian L, Shi S P and Zheng Y H 2025 *Photon. Res.* **13** 3240
[26] Li Q H, Li W, Wang Y F, Wang Y J, Tian L, Shi S P and Zheng Y H 2026 *Laser Photonics Rev.* **20** e01636
[27] Meyer R A 1972 *Appl. Opt.* **11** 613
[28] Xiao Q, Zhou Y and Tao Y 2008 *Chin. Phys. B* **17** 3549
[29] Hong S, Rehman J U, Kim Y S, Cho Y W, Lee S W, Jung H, Moon S, Han S W and Lim H T 2021 *Nat. Commun.* **12** 5211
[30] Luo W, Wu C, Du Y, Zhao C, Yu M, Zhu P and Xu P 2024 *Chin. Phys. B* **33** 100305
[31] Zhang L and Chan K W C 2018 *Sci. Rep.* **8** 11440
[32] Afek I, Ambar O and Silberberg Y 2010 *Science* **328** 879
[33] Zhang L and Chan K W C 2019 *Opt. Commun.* **452** 258
[34] Sanaka K, Resch K J and Zeilinger A 2006 *Phys. Rev. Lett.* **96** 083601
[35] Chen R Y, Luo Y H, Long J B and Liu J Q 2024 *Phys. Rev. Appl.* **22** 054051
[36] Nardelli N V, Reddy D V, Grayson M, Sorensen D and Fortier T M 2026 *Optica Quantum* **4** 138
[37] Zhuang Q T and Shapiro J H 2022 *Phys. Rev. Lett.* **128** 010501
[38] Wu B H, Guha S and Zhuang Q T 2023 *Quantum Sci. Technol.* **8** 035016
[39] Wei R Y, Albarelli F, Li J and Giovannetti V 2024 arXiv:2411.14414 [quant-ph]
[40] Mandel L and Wolf E 1995 *Optical Coherence and Quantum Optics* (Cambridge: Cambridge University Press) Chap. 12
[41] Liu H, Giovannini D, He H Y, England D, Sussman B J, Balaji B and Helmy A S 2019 *Optica* **6** 1349
[42] Amann M C, Bosch T M, Lescure M, Myllylae R A and Rioux M 2001 *Opt. Eng.* **40** 10
[43] Luong D, Lam I W K, Balaji B and Rajan S 2024 *Proc. SPIE* **13048** 130480M
[44] Shi S, Wang Y, Yang W, Zheng Y and Peng K 2018 *Opt. Lett.* **43** 5411
[45] Zhang W, Jiao N, Li R, Tian L, Wang Y and Zheng Y 2021 *Opt. Express* **29** 24315